ChemSusChem

Research Article
doi.org/10.1002/cssc.202200324

Chemistry Europe
European Chemical Societies Publishing

www.chemsuschem.org

On the Durability of Protective Titania Coatings on High-Voltage Spinel Cathodes

Elise R. Østli,[a] Mahsa Ebadi,[a] Yonas Tesfamhret,[b] Mehdi Mahmoodinia,[c] Matthew J. Lacey,[d] Daniel Brandell,[b] Ann Mari Svensson,[a] Sverre M. Selbach,[a] and Nils P. Wagner*[a, e]

TiO_2-coating of $LiNi_{0.5-x}Mn_{1.5+x}O_4$ (LNMO) by atomic layer deposition (ALD) has been studied as a strategy to stabilize the cathode/electrolyte interface and mitigate transition metal (TM) ion dissolution. The TiO_2 coatings were found to be uniform, with thicknesses estimated to 0.2, 0.3, and 0.6 nm for the LNMO powders exposed to 5, 10, and 20 ALD cycles, respectively. While electrochemical characterization in half-cells revealed little to no improvement in the capacity retention neither at 20 nor at 50 °C, improved capacity retention and coulombic efficiencies were demonstrated for the TiO_2-coated LNMO in LNMO||graphite full-cells at 20 °C. This improvement in cycling stability could partly be attributed to thinner cathode electrolyte interphase on the TiO_2-coated samples. Additionally, energy-dispersive X-ray spectroscopy revealed a thinner solid electrolyte interphase on the graphite electrode cycled against TiO_2-coated LNMO, indicating retardation of TM dissolution by the TiO_2-coating.

Introduction

The Co free and environmentally friendly $LiNi_{0.5-x}Mn_{1.5+x}O_4$ (LNMO) is gaining increased attention as a cathode material for the next-generation Li-ion batteries (LIBs). Its high operating voltage (4.7 V vs. Li/Li^+) and capacity (147 $mAh\,g^{-1}$) makes it a good alternative to $LiNi_{1-y-z}Mn_yCo_zO_2$ (NMC).[1] Additionally, the low Ni content, absence of Co, and full utilization of the Li makes LNMO a less expensive and more sustainable option compared to many other high-energy cathode materials that are commercially available today.[2] LNMO has, however, still some issues that limit its use. The commercially available electrolytes, consisting of $LiPF_6$ salt in carbonate solvents [e.g., ethylene carbonate (EC), diethyl carbonate (DEC), dimethyl carbonate (DMC)] have too narrow electrochemical stability windows and are therefore not thermodynamically stable at the high operating voltage of LNMO.[3,4] In contrast to the solid electrolyte interphase (SEI) that is formed on anode materials such as graphite, the cathode electrolyte interphase (CEI) that is formed on LNMO upon battery cycling is less stable, even though it has been demonstrated that LNMO forms a more stable CEI compared to layered high-voltage cathode materials.[5] The lack of a stable CEI leads to continuous decomposition of the electrolyte as the battery is cycled. The $LiPF_6$ salt can furthermore form HF in the presence of trace amounts of water, and coupled $LiPF_6$ and EC decomposition can lead to increased HF formation.[6] HF can in turn attack the active material and lead to transition metal (TM) ion dissolution, where Mn and Ni ions migrate over to the anode and destabilize the SEI layer and cause additional electrolyte degradation and Li consumption.[7] In addition to HF attack, the disproportionation reaction ($2Mn^{3+} \rightarrow Mn^{2+} + Mn^{4+}$) has been reported to be one of the main reasons for TM dissolution in the spinel cathode materials.[8] LNMO, in contrast to $LiMn_2O_4$ (LMO), has most of its Mn in the tetravalent state and therefore does not have problems related to the disproportionation reaction to the same extent. However, non-stoichiometric and/or oxygen-deficient LNMO will contain some Mn^{3+} due to charge compensation, and dissolution of both Mn^{2+} and Mn^{3+} from LNMO has been reported in the literature, making TM dissolution a significant issue also for LNMO.[9–11] Although morphology optimization can reduce the surface area in contact with the electrolyte and minimize these parasitic side reactions, this in itself is not sufficient to allow full commercialization of LNMO, in particular at elevated temperatures where the LNMO/electrolyte interface is highly unstable.[7] Several strategies have thus been extensively researched to mitigate

[a] E. R. Østli, Dr. M. Ebadi, Prof. A. M. Svensson, Prof. S. M. Selbach, Prof. N. P. Wagner
Department of Materials Science and Engineering
NTNU Norwegian University of Science and Technology
7491 Trondheim (Norway)
E-mail: nils.p.wagner@ntnu.no
[b] Y. Tesfamhret, Prof. D. Brandell
Department of Chemistry – Ångström Laboratory
Uppsala University
Box 538, 75121 Uppsala (Sweden)
[c] Dr. M. Mahmoodinia
Department of Chemical Engineering NTNU Norwegian University of Science and Technology
7491 Trondheim (Norway)
[d] Dr. M. J. Lacey
Scania CV AB 151 32
Södertälje (Sweden)
[e] Prof. N. P. Wagner
SINTEF Industry 7491
Trondheim (Norway)

Supporting information for this article is available on the WWW under https://doi.org/10.1002/cssc.202200324

the unwanted reactions on the LNMO surface, such as surface coatings, doping, and electrolyte additives.[12]

Next to the implementation of alternative electrolyte and film-forming additives, the strategy of applying a surface coating on the LNMO surface, and in this way form an artificial CEI, has been shown to impede the unwanted side reactions. A large variety of coating materials, for example oxides, fluorides, and phosphates, have been investigated for this purpose.[13] Oxide coating materials such as Al_2O_3,[14] TiO_2,[15,16] and SiO_2[17] all have the benefits of chemical simplicity, non-toxicity, and abundance of the constitutive elements. They can be applied by several coating techniques and therefore be designed accurately for their use. This flexibility enables cost-efficient implementation of the coating, as it is not necessary to choose complicated and expensive coating techniques and/or precursors. Many oxide coating materials have, however, limited Li-ion and electric conductivity and can form a Li diffusion barrier that increases the impedance of the cell.[13,18] A merit of TiO_2 as a coating material candidate is the relatively high Li-ion conductivity compared to, for example, Al_2O_3. The rutile and anatase phases have been reported to have diffusion coefficients of $1\times10^{-6}\,cm^2\,s^{-1}$ and $4.7\times10^{-12}\,cm^2\,s^{-1}$ at 300 K, respectively.[19,20] Furthermore, being electrochemically active between 1.5 and 2 V vs. Li, TiO_2 has been suggested as a high-rate anode material for Li-ion batteries.[21–23] For comparison, amorphous Al_2O_3 has a reported diffusion coefficient of $5.94\times10^{-17}\,cm^2\,s^{-1}$ at 300 K.[13,24] Amorphous TiO_2 has a higher measured Li-ion diffusivity than anatase,[21] and a substantially smaller bandgap (3.2–3.4 eV)[25,26] relative to amorphous Al_2O_3 (6.9 eV).[27] The bandgap of LNMO, calculated to be 0.49–0.72 eV depending on the crystal structure,[28] is thus substantially lower than for all the afore-mentioned coating materials, and even though TiO_2 is a better ionic and electronic conductor than some of the other oxide coating candidates, the low electronic conductivity still makes the thickness critical to allow Li-ion transport through the coating. Atomic layer deposition (ALD) is a coating technique that allows for accurate control of the coating thickness and ensures uniform deposition.[29] The possibility to deposit a large variety of functional materials at low deposition temperatures has made ALD an attractive technique to modify interfaces in both LIBs and other systems.[30,31] It is therefore an excellent coating technique for studying the effects of ultra-thin coatings.

The application of TiO_2-coating has been shown to improve the electrochemical properties of several cathode materials. Zhou et al. reported TiO_2-coated $LiCoO_2$ (LCO) electrodes to yield a 40% higher capacity retention over 100 cycles compared to the uncoated LCO electrode, where the cells were cycled between 3.0 and 4.5 V.[32] This was attributed to increased resistance to interfacial side reactions by the applied coating, which form a stable and conducting TiF_x interphase by reaction with HF in the electrolyte. Similarly, Cheng et al.[33] found improved capacity retention at long-term cycling in half-cells for TiO_2-coated LCO. The TiO_2-coating was, however, found to be unstable as it participates in the redox reaction with the underlying cathode material and thus only offers temporary protection from TM dissolution and HF attack. The TiO_2-coating was furthermore found to gradually be removed from the LCO surface upon cycling. NMC-622 coated with amorphous TiO_2 via ALD was investigated by Qin et al.,[34] and improved capacity retention and higher discharge capacity was found for the 5 nm thick TiO_2-coating compared to the bare NMC-622 both at 25 and 55 °C. Lu et al.[35] compared TiO_2-coating and Ti surface doping of LMO, and found that both ALD surface coating and surface doping of LMO improved the high-temperature (55 °C) cycling performance in half-cells. ALD TiO_2 and Al_2O_3-coating of LMO thin film electrodes were investigated by Mattelaer et al.[36] with specific focus on rate capability, and TiO_2-coating was shown to improve the kinetics of the electrode in contrast to Al_2O_3, which dramatically worsens it. The improved kinetics for the TiO_2-coated LMO was attributed to a reduction of CEI formation combined with the Li-ion conducting nature of TiO_2.

The high reactivity between LNMO and the electrolyte demands a stable coating material, in particular at higher temperatures where the LNMO/electrolyte interface is particularly unstable.[37] Several studies of TiO_2-coated LNMO have reported on improved cycling stability for the coated samples, indicating that TiO_2 can be sufficiently stable to protect the highly reactive LNMO surface. TiO_2 surface modification of LNMO applied by a solid-state route, resulting in an island-type coating consisting of Ti-rich particles on the LNMO surface, has been evaluated by Wang et al.[38] Although the TiO_2-coating induced a subtly increased polarization and unchanged capacity retention at 25 °C, the TiO_2-coated LNMO displayed improved capacity retention at 55 °C and reduced Mn dissolution compared to the bare LNMO. Successful wet chemical TiO_2-coating of LNMO was reported by both Hao and Bartlett[16] and Tao et al.[39] The former reported on improved capacity retention at 55 °C and a maintained structural integrity for the TiO_2-coated sample. Tao et al.[39] additionally reported on outstanding rate capability for the TiO_2-coated LNMO. Cho et al.[40] coated LNMO nanowires with TiO_2 and Al_2O_3 by ALD. The high-surface-area nanowires displayed detrimental interfacial side reactions when not protected by the ALD coating. Both the Al_2O_3- and the TiO_2-coating improved the rate capability and cycling stability while reducing the TM dissolution.

From previous studies, it is clear that TiO_2 shows great promise as a protective surface coating on LNMO. TiO_2 is, however, found to be a HF scavenger rather than a HF barrier and will therefore react with HF and only offer temporary protection from HF attack.[41] It is furthermore not well understood how the TiO_2-coating is changing over time, and how robust it is under long-term cycling, as the majority of published studies do not emphasize post-mortem characterization but rather focus on electrochemical characterization, and mainly in half-cell configuration only.[42] The large excess in available Li from the often employed thick Li metal electrodes will mask certain degradation effects, such as capacity decay caused by Li inventory loss. On the other hand the highly reactive Li metal electrode can induce side reactions such as electrolyte consumption by repeated SEI formation as well as short circuiting by mossy Li plating.[43] It has furthermore been found that the choice of cathode material will impact how the Li deposits upon battery cycling, and that LNMO causes higher

Li overpotentials than, for example NMC622 and $LiFePO_4$ (LFP).[44] Further knowledge of the long-term protection of the TiO_2-coating, in particular at higher temperatures and in full-cell configuration where the amount of cyclable Li is limited, is necessary to gain knowledge of the feasibility of TiO_2-surface coatings as a solution to the TM dissolution problem. In the current study, ultra-thin ALD TiO_2-coatings were deposited on commercial LNMO powder. Three coating thicknesses of <1 nm were investigated, and the effect on electrochemical properties in half- as well as full-cell configuration was studied both at 20 and 50 °C. New insights on the protective properties and durability of the TiO_2-coating were obtained by post-mortem characterization by scanning electron microscopy (SEM) and energy-dispersive X-ray spectroscopy (EDX), as well as initial CEI investigations by X-ray photoelectron spectroscopy (XPS).

Results and Discussion

Materials Characterization

The secondary LNMO particles were coated with ultra-thin TiO_2 layers by ALD. Three TiO_2 coating thicknesses were applied, corresponding to 5, 10, and 20 ALD cycles of $TiCl_4$- and H_2O-precursor exposure, hereafter named 5 ALD TiO_2, 10 ALD TiO_2, and 20 ALD TiO_2, respectively. X-ray diffraction (XRD) of all samples was performed to ensure that the coating procedure had not altered the LNMO bulk phase or introduced crystalline impurity phases that would suggest segregation of TiO_2 rather than a homogeneous coating. The X-ray diffractograms are depicted in Figure 1a (full pattern Rietveld refinement in Figure S1, Supporting Information). All four samples show reflections that can be indexed as phase pure LNMO with the space group *Fd*-3 *m*, which is a disordered spinel structure, where the Ni and Mn cations are randomly distributed in the 16*d* sites while Li and O ions occupy the 8*a* and 32*e* sites, respectively. The XRD results show no change in the LNMO bulk crystal structure by the coating deposition. This is expected since the bulk cation diffusion is negligible at the low deposition temperature (120 °C). In addition to XRD, Raman spectroscopy can provide information about the degree of ordering in the LNMO spinel. Even though Raman spectroscopy is relatively surface-sensitive, with a probing depth of 20–300 nm,[45,46] the amorphous and ultra-thin TiO_2-coating is not detectable. From the Raman spectra in Figure 1b, one can see that the main features are very similar for all four powder samples. The peak at 165 cm^{-1} and slightly more diffuse peak at 407 cm^{-1} are indications of partial ordering in the LNMO structure.[45,47] The relatively low intensity of these peaks is, however, not indicating complete ordering of the Ni and Mn. No changes in peak positions between the samples can be observed, further confirming that the LNMO has not been

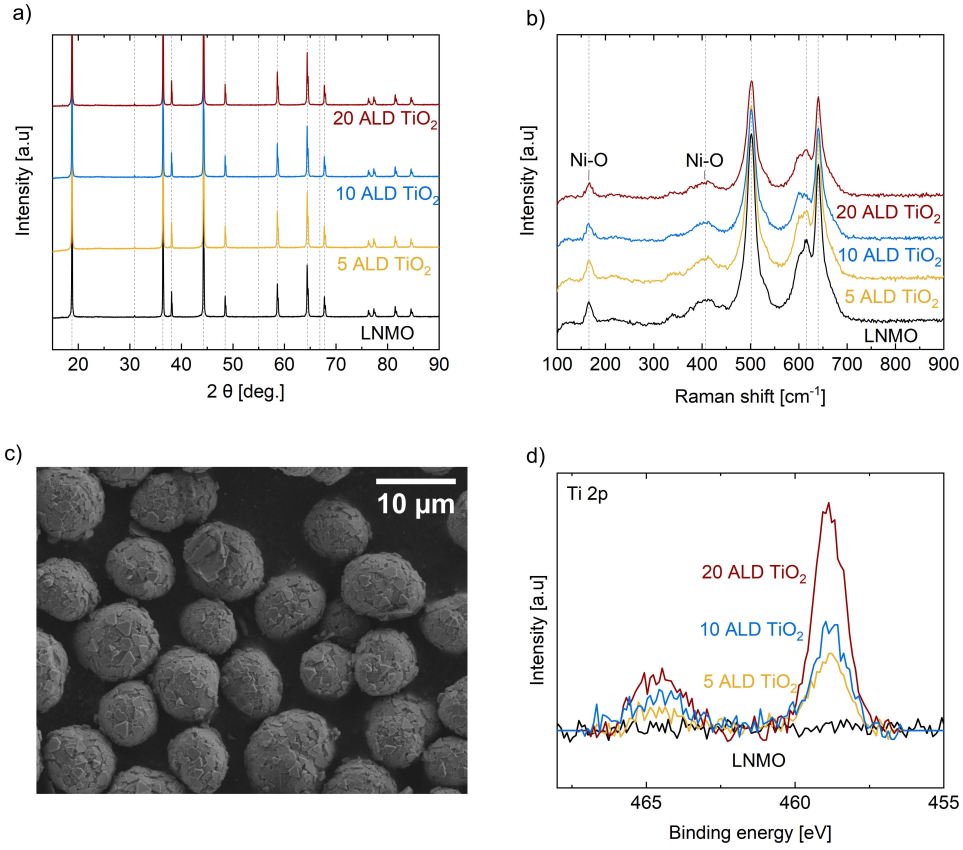

Figure 1. (a) X-ray diffractograms, (b) Raman spectra, and d) Ti 2p XPS spectra from the uncoated LNMO (black), 5 ALD TiO_2 (yellow), 10 ALD TiO_2 (blue), and 20 ALD TiO_2 (red). (c) SEM image of the uncoated LNMO powder.

altered by the coating deposition. The peak intensities vary slightly between the samples, but this can be explained by surface effects rather than change in the bulk LNMO phase. The surface morphology of the LNMO powder, depicted in the SEM image in Figure 1c, shows that the LNMO particles are spherical with a particle size of approximately 10 μm. The particle surface consists of faceted grains that form a rather rough outer layer. This rough surface structure can explain the small variations in peak intensities observed in the Raman spectra, as the presence of edges and surface defects can give rise to such variations in peak intensities. All the four powder samples were also analyzed by XPS to verify the presence of Ti on the surface of the TiO_2-coated powder sample. The Mn 2p, Ni 2p, and survey spectra are included in Figure S2 (Supporting Information). The Ti 2p spectra of all four samples are displayed in Figure 1d. There is no Ti 2p signal from the uncoated LNMO (black), while the peak intensity increases with the number of ALD cycles applied [5 ALD TiO_2 (yellow) < 10 ALD TiO_2 (blue) < 20 ALD TiO_2 (red)].

The characterization of ultra-thin coatings on a particle surface is quite challenging, since the coating will be difficult to detect by techniques that are not sufficiently surface-sensitive. By combining transmission electron microscopy (TEM) imaging and inductively coupled plasma-mass spectrometry (ICP-MS), the homogeneity and the degree of coating coverage for such ultra-thin coatings can be investigated. From the TEM imaging one can obtain a visual estimate of the coating thickness and uniformity from a few particles. Although this is a very accurate technique, the few particles that are being examined are not necessarily representative for all the coated particles. By dissolving the four powder samples and performing ICP-MS analysis, the average Ti content for the four samples was obtained. From the measured Ti amounts, the Brunauer–Emmett–Teller (BET) surface area of the LNMO powder (measured to be 0.276 $m^2 g^{-1}$), and the density of amorphous TiO_2 (analyzed by Anderson et al. to be 3.82 $g cm^{-3}$),[48] a TiO_2 coating thickness was calculated. Comparing the calculated thickness to the observed thickness from TEM ensures accurate and representative estimates of the coating thickness. The cross-section of a 20 ALD TiO_2 particle was examined with TEM, and a STEM micrograph of the particle surface is shown in Figure 2a. The crystalline LNMO bulk phase is clearly visible. Along the faceted surface there is a slightly brighter layer a bit less than 1 nm in thickness. From the electron energy loss (EELS) spectra in Figure 2b–e, it is confirmed that this surface layer contains Ti and O. TiO_2 grown by ALD at temperatures below 200 °C has been shown to be amorphous.[49,50] Even though the thin surface layer appears to have a crystalline structure based on the STEM images, it is important to point out that the sample is not necessarily angled along the grain and the thin surface layer therefore can appear to be crystalline because the crystalline LNMO phase may be visible through the coating layer. An additional STEM image is included in Figure S3 (Supporting Information).

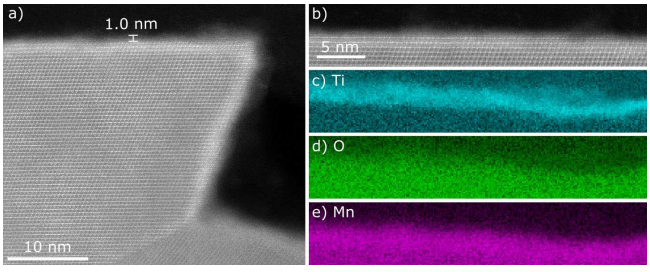

Figure 2. STEM results from the cross-section of a 20 ALD TiO_2 particle before cycling. (a) Annular dark-field (ADF)-STEM micrograph showing the uniform coating with a thickness of less than 1 nm. (b) ADF-STEM image with atomic resolution showing the TiO_2-coating on a facet. (c–e) Corresponding EELS elemental maps from the Ti-K, O-K, and Mn-$L_{2,3}$ core loss.

The ICP-MS results are presented in Table 1. The calculated TiO_2 thicknesses based on the measured Ti contents are 0.2, 0.3, and 0.6 nm for 5, 10, and 20 ALD TiO_2, respectively. The calculated coating thickness of 20 ALD TiO_2 corresponds reasonably well with the observed coating thickness from the STEM micrograph in Figure 2a. A visual estimate of the coating thickness from a STEM micrograph is challenging for coatings of < 1 nm thickness. Furthermore, when it comes to such ultra-thin coatings, it is difficult to conclude on the degree of crystallinity. However, it can be concluded that the even and ultra-thin layer covering the LNMO particle uniformly consists of Ti and O. The combined STEM and ICP-MS results indicate certainly that the coating layer is homogeneous and evenly distributed on the LNMO particle.

To summarize, the initial materials characterization shows that the TiO_2 deposition has been successful, yielding a coating thickness of approximately 0.2, 0.3, and 0.6 nm TiO_2 on the 5, 10, and 20 ALD TiO_2 samples, respectively. The coating deposition has not altered the LNMO bulk crystal structure.

Electrochemical characterization

Rate testing of half-cells containing the LNMO and 5, 10, and 20 ALD TiO_2 samples was conducted at 20 °C. The charge–discharge curves for the 3rd cycle at a C-rate of C/10 are shown in Figure 3a. Voltage profiles for all samples with one representative cycle for each C-rate (C/5–2C) are included in Figure S5 (Supporting Information). The characteristic LNMO profile is visible for all 4 samples, with a small plateau around 4 V vs. Li/Li^+ and two main plateaus at around 4.7 V vs. Li/Li^+. The 4 V plateau can be attributed to Mn^{3+}/Mn^{4+} activity, and the 4.7 V plateaus are due to $Ni^{2+}/Ni^{3+}/Ni^{4+}$ activity.[51] The clear

Table 1. Ti content measured by ICP-MS and the corresponding calculated TiO_2 thickness based on a surface area measured by BET to be 0.276 $m^2 g^{-1}$ and the density of amorphous TiO_2 of 3.82 $g cm^{-3}$.[48]

Sample	Ti content[a] [mg kg^{-1}]	Calculated coating thickness [nm]
LNMO	0.9	–
5 ALD TiO_2	134	0.2
10 ALD TiO_2	208	0.3
20 ALD TiO_2	380	0.6

[a] RSD 15–25 %

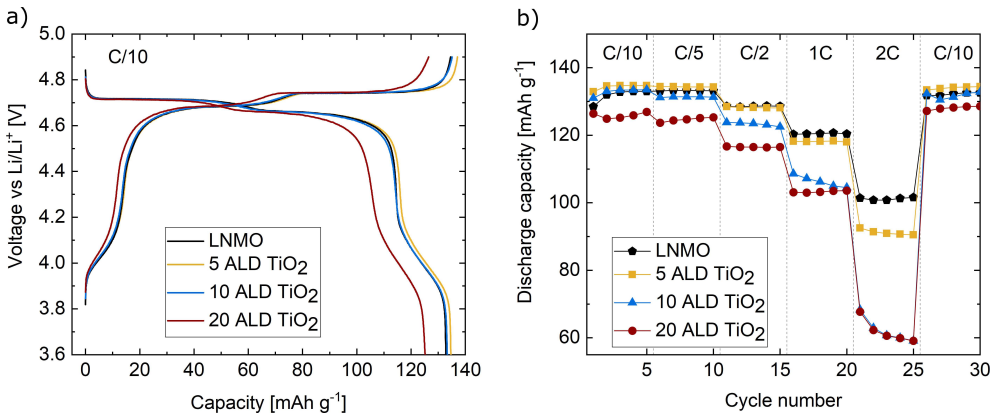

Figure 3. (a) Charge–discharge curves from 3rd charging cycle at C/10 and (b) discharge capacity vs. cycle number for rate testing of half-cells containing LNMO (black) 5 ALD TiO_2 (yellow), 10 ALD TiO_2 (blue), and 20 ALD TiO_2 (red) at 20 °C.

4 V plateau can be explained by the Mn-content in the LNMO used in this study ($LiNi_{0.43}Mn_{1.57}O_4$), which is slightly higher than for stoichiometric LNMO ($LiNi_{0.5}Mn_{1.5}O_4$), yielding a larger amount of Mn^{3+} that contributes to the capacity. 5 ALD TiO_2 has a slightly higher discharge capacity (135 mAh g^{-1}) compared to the uncoated LNMO and the 10 ALD TiO_2 (133 mAh g^{-1}). These are very small variations, and the discharge capacity can be considered as unaltered by the two thinnest TiO_2-coatings. The 20 ALD TiO_2 (125 mAh g^{-1}) displays a more significant decrease in capacity. The decrease in capacity for the thicker TiO_2-coating is not completely unexpected, as amorphous TiO_2 has a limited Li-ion diffusivity and electronic conductivity. The effect is, however, not very dramatic at lower C-rates. At higher C-rates the effect of the TiO_2-coating on the discharge capacity is more pronounced, as can be seen in Figure 3b where the discharge capacity is plotted vs. cycle number. When a C-rate of C/2 is applied, the 10 ALD TiO_2 capacity is reduced compared to the uncoated LNMO and 5 ALD TiO_2, and at 1C both the 10 and 20 ALD TiO_2 are lowered to just above 100 mAh g^{-1}, while the 5 ALD TiO_2 and LNMO are still yielding a discharge capacity of around 120 mAh g^{-1}. At 2C, the discharge capacities of both the 20 and 10 ALD TiO_2 are reduced to 60 mAh g^{-1}. The 5 ALD TiO_2 is yielding a capacity of 90 mAh g^{-1}, while the uncoated LNMO is performing best with a discharge capacity of above 100 mAh g^{-1}. It should be mentioned that higher capacities could be obtainable with different cut-off voltages. When the C-rate is reduced to C/10 after cycle number 25, the initial discharge capacity is regained for all samples, indicating that no material degradation occurred during the rate tests. The coulombic efficiencies at the different C-rates are shown in Figure S4 (Supporting Information). Little to no difference can be seen between the coulombic efficiencies of the four samples. The coulombic efficiencies are higher for the higher C-rates, which can be due to the shorter time spent on the high potentials where the electrode/electrolyte interface is at its most unstable, thus allowing fewer unwanted side reactions to occur. Even though the decrease in capacity induced by the TiO_2-coating is not very dramatic, especially at the lower C-rates, it is worth mentioning that the reduction in rate performance due to the TiO_2-coating is important to note as the fast Li-diffusion of LNMO is one of its strong suits.[52]

To gain further knowledge of the electrochemical properties of the TiO_2-coatings, long-term galvanostatic charge–discharge cycling of half-cells was performed at 20 and 50 °C. The cells were cycled with a C-rate of C/2 with two cycles of C/10 every 25th cycle. The discharge capacities and coulombic efficiencies of all the four samples cycled at 20 °C are shown in Figure 4a. During the first 60 cycles, the capacity is showing the same trend as for the rate testing, where the 5 and 10 ALD TiO_2 are behaving similarly to the uncoated LNMO (stable cycling at around 130 mAh g^{-1}), while the 20 ALD TiO_2 is yielding a slightly lower capacity (120 mAh g^{-1}). All cells are displaying stable cycling until 60 charging cycles, where 10 ALD TiO_2 is starting to decay at C/2. The capacity is, however, regained for all samples at the slower C/10 cycles, also after the point of capacity decay. This indicates that the origin of capacity decay is kinetic limitations originating from, for example, film formation from electrolyte decomposition, and not from degradation of the active material. Li metal is known to continuously form a SEI layer with cycling, something that can lead to Li passivation and partly be responsible for the observed capacity decay and large variety in the capacity decay onset.[53] The coulombic efficiencies at room temperature stabilize at 99.5 % for all the samples after the formation cycles.

At 50 °C, the TiO_2-coated LNMO samples yield a capacity that is 5–10 mAh g^{-1} higher than for the uncoated LNMO. The difference between 20 and 50 °C is particularly notable for the 20 ALD TiO_2, which goes from an average capacity of 120 mAh g^{-1} at 20 °C to 130 mAh g^{-1} at 50 °C. The Li-diffusion barrier that the TiO_2-coating creates is, as expected, less prominent at higher temperatures. The difference in capacity between the coated and uncoated LNMO can additionally point towards a reduced reactivity of the LNMO surface due to the TiO_2-coating. The onset for capacity decay varied greatly between the cells, and average values for 3–5 cells with standard deviations are included in Figure S6 (Supporting Information). Note that, as for the measurements at 20 °C, the

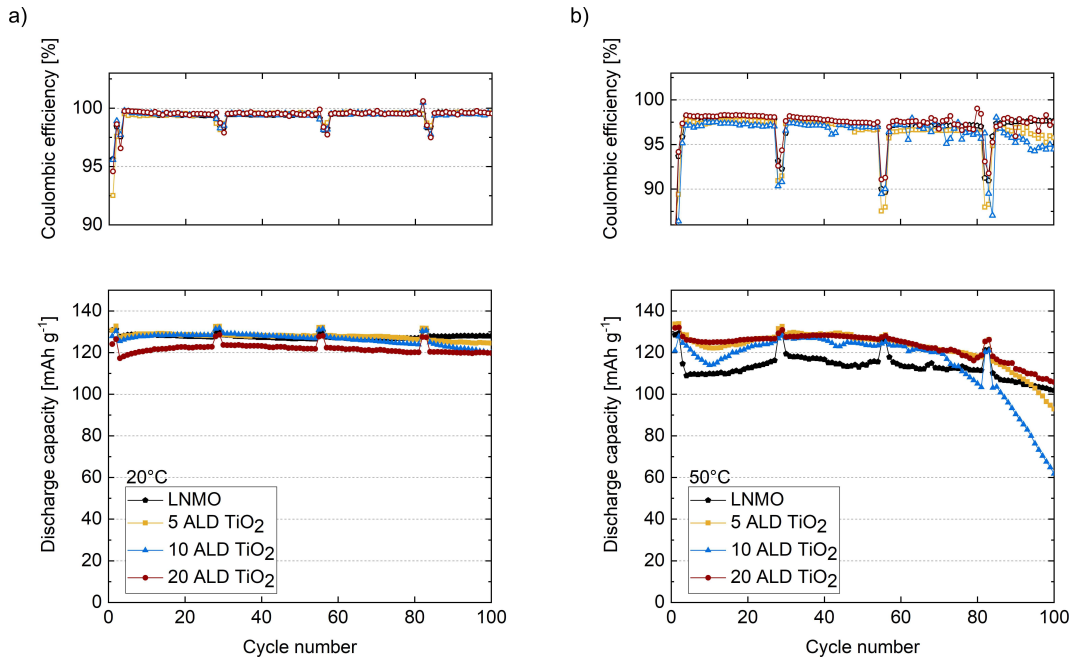

Figure 4. Coulombic efficiency and discharge capacity at (a) 20 °C, and (b) 50 °C for uncoated LNMO (black) 5 ALD TiO_2 (yellow), 10 ALD TiO_2 (blue), and 20 ALD TiO_2 (red). The cells were cycled at a C-rate of C/2 with two C/10 cycles every 25th cycle.

initial capacity is regained at the slower charging cycles also here, indicating that the dramatic capacity decay initiating after 80 charging cycles is more likely due to electrolyte degradation and film formation on the Li electrode, which increases the resistance in the cell, rather than from irreversible degradation of the active material. Increased scatter in the coulombic efficiency values from 60 cycles onwards supports this argument. A test set-up employing Li metal as anode and carbonate-based electrolytes is, as previously discussed, not suitable to gain information about prolonged cycling stability. The Li metal is very reactive and will introduce degradation mechanisms, which leads to increased cell impedance and electrolyte degradation, such as continuous SEI formation. Additionally, at 50 °C, the $LiPF_6$ salt in the electrolyte is unstable, leading to salt decomposition and additional electrolyte consumption.[54]

To further investigate the TiO_2-coatings effect on the cycling stability, full-cells containing LNMO and 20 ALD TiO_2 were cycled against graphite both at 20 and 50 °C. The 20 ALD TiO_2 was chosen due to its most probable complete coating coverage of the LNMO particles with its coating thickness of around 0.6 nm. Hence, limited direct contact between the LNMO and the electrolyte can be assumed, and additional information about the coating's effect on the TM dissolution can be gained by post-mortem analysis on cycled electrodes.

After four formation cycles at C/10 and C/4 the full-cells were cycled at C/2 with two slow charging cycles at C/10 every 25th cycle. The discharge capacity for the 200 first cycles at 20 °C and the corresponding coulombic efficiencies are shown in Figure 5a,b, respectively. LNMO has a higher initial capacity (120 mAh g^{-1}) than 20 ALD TiO_2 (100 mAh g^{-1}), and the first cycle losses are 19.5 and 21.4 mAh g^{-1}, respectively. The 20 ALD TiO_2, however, shows improved cycling stability. While the reversible capacity of the uncoated LNMO has decayed by 20% of initial capacity after only 70 cycles, the 20 ALD TiO_2 retains more than 80% of the initial reversible capacity up until 120 cycles. The difference in obtained capacity at low (C/10) and high (C/2) rates is steadily increasing. This is visible in Figure 5a but becomes clearer in Figure 5b where the drop in coulombic efficiency when switching from low to high rate is steadily increasing for the uncoated sample. This indicates more sluggish kinetics that might originate from a formation of a thicker CEI on the uncoated LNMO or a more resistive SEI on the corresponding graphite anode. The uncoated sample showed average coulombic efficiency values of 99.5% for the first 50 cycles. Afterwards the values scattered between 99.1 and 99.9%, where the lowest values upon changing of C-rate is declining with increasing number of charging cycles (indicated with gray arrow). The 20 ALD TiO_2 cell showed stable coulombic efficiency values approaching high values of 99.7% after 10 cycles and at 96.5% upon changing of C-rate (pink arrow). Combined, these results indicate that although the TiO_2-coating reduces the obtainable capacity by increased overpotential, it also reduces the irreversible Li loss and the formation of impeding interface layers due to side reactions at 20 °C. This is further illustrated in the charge–discharge curves of the C/10 cycles from cycle number 31 to cycle number 193, presented in Figure 5c,d for uncoated LNMO and 20 ALD TiO_2, respectively. Both the LNMO and 20 ALD TiO_2 display the expected voltage profile from a LNMO||graphite full-cell,[55] although the 20 ALD TiO_2 clearly has a larger overpotential at the 31st cycle due to the dense TiO_2-coating. This is also evident by comparing the

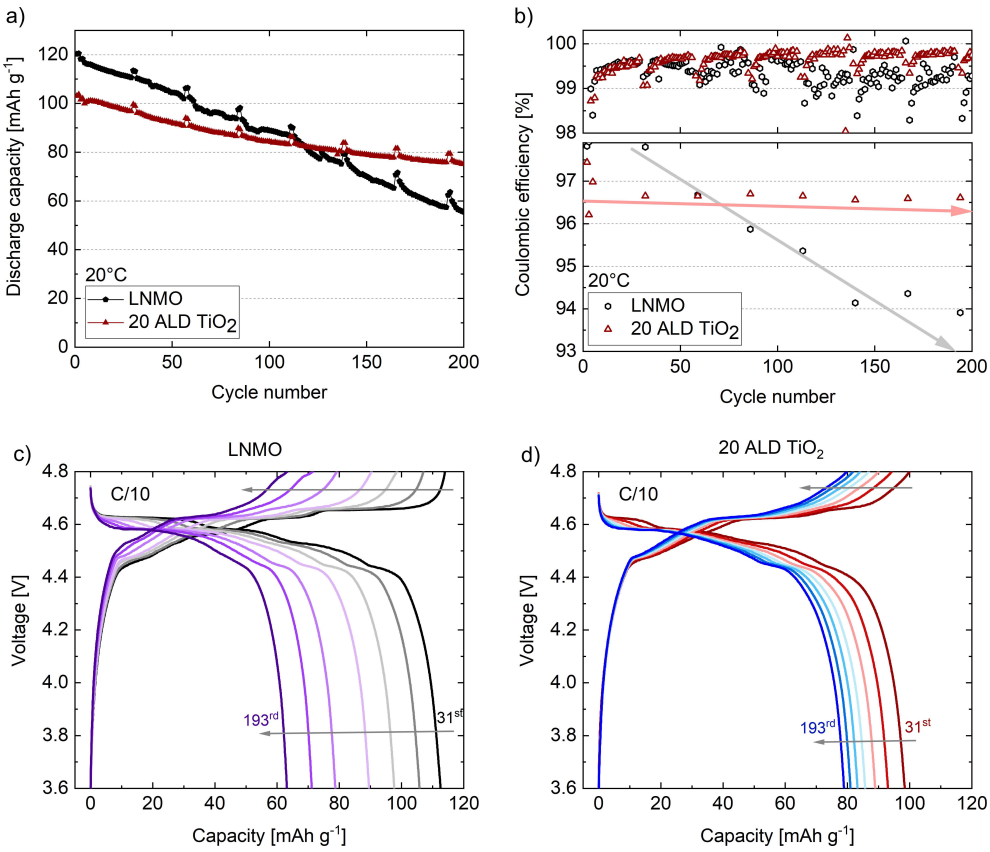

Figure 5. (a) Discharge capacity and (b) coulombic efficiency per cycle for LNMO (black) and 20 ALD TiO_2 (red) full-cells with graphite counter electrode. The lower coulombic efficiency values upon change in C-rate are shown in the lower part of (b) with trends for LNMO and 20 ALD TiO_2 indicated by arrows (gray and pink, respectively). After the four formation cycles of C/10 and C/4, the cells are cycled at C/2 with two C/10 cycles every 25th cycle. Charge–discharge curves of the second C/10 cycle from the 31st to the 193rd charging cycle of (c) LNMO and (d) 20 ALD TiO_2.

two first formation cycles of both the samples, presented in Figure S7 (Supporting Information). The negative/positive (N/P) ratios of both cells are approximately 1.16. The 20 ALD TiO_2 sample will, however, have a slightly higher practical N/P ratio due to the higher polarization. This results in the shorter plateau a bit above 4.6 V. With increasing number of charge discharge cycles, it is clear that the LNMO has a much more dramatic reduction in capacity than the 20 ALD TiO_2, and after 193 charging cycles, the uncoated LNMO has a larger overpotential and 20 mAh g^{-1} lower capacity than the 20 ALD TiO_2. The faster capacity decay for the uncoated LNMO can be attributed to Li inventory loss caused by side reactions that trap the cyclable Li. The increased overpotential in the LNMO cell with increasing number of charge discharge cycles can furthermore be due to formation of interface layers on the electrodes that both impede and trap the cyclable Li-ions.

At 50 °C, no improvement in the capacity retention could be found for the TiO_2-coated LNMO, as illustrated in Figure S8 (Supporting Information). Both LNMO and 20 ALD TiO_2 operate poorly under these conditions, and large variety between the different parallells was observed. This is not completely unexpected since the LNMO||graphite cell is known to be unstable at elevated temperature, and storing such cells at elevated temperatures can lead to formation of inactive surface films on both the graphite and the LNMO surface that lead to increased impedance in the cell.[56] Reducing the surface reactivity of LNMO by applying TiO_2-coating is thus not sufficient to stabilize the LNMO||graphite cell at elevated temperatures.

The surface of uncoated LNMO and 20 ALD TiO_2 was characterized by XPS. Pristine electrodes, electrodes charged to 4.9 V vs. Li/Li^+ at C/10 (charged), and electrodes charged to 4.9 V vs. Li/Li^+ at C/10 and discharged to 3.6 V vs. Li/Li^+ at C/10 (charged + discharged) were analyzed for both samples. The F 1 s and O 1 s spectra for all samples are presented in Figure 6. For both the uncoated LNMO and the 20 ALD TiO_2, the F 1 s spectra show one distinct peak (688 eV) for the pristine electrode and the charged electrode, indexed to the PVDF-HFP (poly(vinylidene fluoride-co-hexafluoropropylene)) binder.[57] The uncoated LNMO charged + discharged electrode has an additional peak with binding energy (BE) around 685.6 eV, which is assigned to LiF (685.1 eV),[58] with some possible contribution from $Li_xPF_yO_z$ (686.5 eV).[59] The 20 ALD TiO_2, on the other hand, does not display the clear LiF peak, but instead has a less prominent peak at lower BE (684.7 eV) that can be assigned to $TiOF_2$.[60] This indicates that fluorination of the TiO_2 coating occurs already after the first charging cycle. It furthermore indicates that the amount of $LiPF_6$ decomposition

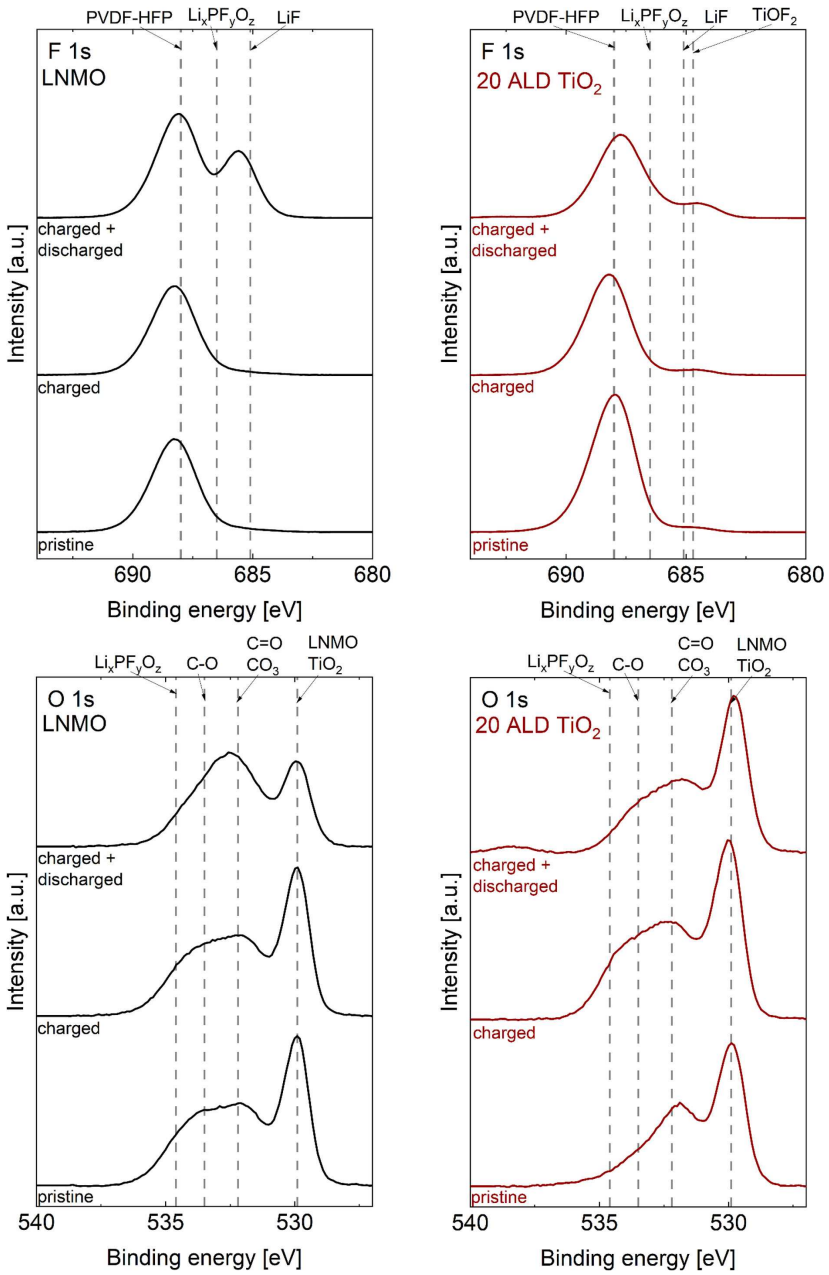

Figure 6. XPS F1s and O1s spectra from analysis of electrodes containing LNMO (black) and 20 ALD TiO_2 (red) electrodes both before cycling (pristine), after one charge, and after one full charging cycle.

products such as LiF and $Li_xPF_yO_z$ is lower on the TiO_2-coated sample. The O 1 s spectra of all samples show a distinct lattice metal oxide peak (529.9 eV), that can be assigned to, for example, TiO_2 and LNMO. The surface-related peaks (C–O at 533.5 eV, C=O/CO_3 at 532.2 eV, $Li_xPF_yO_z$ at 534.6 eV)[47,58] are unchanged for the three 20 ALD TiO_2 samples, apart from a slight increase in the peak intensity related to the C–O for the cycled electrodes. The relative intensity ratio between the lattice metal oxide peak and the surface-related peaks are furthermore unchanged for the TiO_2-coated samples. Uncoated LNMO has a more pronounced change in the intensity ratio. The surface-related peaks dominate to a larger extent, in particular after one charge and discharge, indicating the formation of a thicker CEI layer on the uncoated LNMO surface. This is supported by the Ti 2p spectra, presented in Figure S9 (Supporting Information), where the Ti 2p peak intensities are uncanged for all 20 ALD TiO_2 samples.

The full-cells were opened post-mortem after 210 cycles, and the graphite electrodes from both the uncoated LNMO and 20 ALD TiO_2 full-cells were analyzed by SEM and EDX. Although exact quantification with this technique is challenging, EDX is excellent for qualitative and semi quantitative analyses and element mapping of sample surfaces. Note that the color intensity in the EDX maps does not reflect the concentration of

the elements, but only illustrates the position of the elements on the sample. The secondary electron (SE) images of the graphite surfaces and associated X-ray element maps for C, Mn, F, and O are shown in Figure 7a,b for the graphite electrodes from the uncoated LNMO and 20 ALD TiO_2 full-cells, respectively. Both graphite electrodes have similar morphology with particles that are covered in a surface film that leads to some degree of charging. The C maps (purple) overlap accurately with the particles visible in the SE images of both graphite electrodes. Based on the EDX maps, Mn (teal) is detected on both of the graphite surfaces. The lack of surface sensitivity of the Mn K signal due to its high energy (5.9 keV) can lead to misleading elemental mapping. Thus, even though Mn appears to be mainly distributed in between the graphite particles, the Mn is more likely distributed uniformly on the graphite surface. This can be confirmed by mapping the Mn L signal for both samples, which will give more surface sensitive information. In Figure S10 (Supporting Information), the Mn elemental maps based on the Mn L signal are shown and confirm that the Mn is distributed evenly on the graphite particle surface. F (orange) can be detected on both graphite samples. It has been shown that the graphite SEI consists of several F-containing species, such as LiF and $Li_xPF_yO_z$, in addition to $LiPF_6$ salt from the electrolyte.[61] F is detected on the whole graphite electrode surface, with some brighter spots that correlate well with areas in the SE images with increased charging. O (red) is detected on both graphite surfaces and can originate from the many decomposition products of $LiPF_6$ and EC, such as Li_2CO_3 or CH_3OCO_2Li.[62]

A semi quantitative analysis to gain information about the difference in SEI composition and thickness can be conducted by comparing the calculated Mn/C and F/C ratios between the two samples. For the graphite that has been cycled against LNMO, the Mn/C and F/C ratios are 0.012 and 0.232, respectively. The graphite cycled against 20 ALD TiO_2, on the other hand, has Mn/C and F/C ratios of 0.004 and 0.075. The surface of the graphite cycled against the uncoated LNMO has thus approximately 3 times higher Mn/C and F/C ratio than the graphite that has been cycled against 20 ALD TiO_2, strongly indicating increased electrolyte degradation or the formation of a thicker SEI that contains more Mn for the former. This suggests that even though the TiO_2-coating is not hindering the TM dissolution completely, it is reducing or retarding it.

The EDX spectra based on the EDX maps of both graphite electrodes are presented in Figure 8a,b for the graphite cycled against LNMO and 20 ALD TiO_2, respectively. Ni, Fe, and Cu can be detected on both electrodes. The Cu signal most likely originates from the Cu current collector. The analyzed electrodes have a graphite coating of only a few µm, and the Cu current collector can therefore be "visible" through the graphite. The Ni signal can originate from dissolved Ni from the LNMO, as Ni dissolution has been reported in LNMO||graphite cells.[7] The presence of Fe can be an indication that some corrosion of the coin cell parts occurs during battery cycling, and it is possible that some of the detected Mn and Ni stems from steel corrosion. It is, however, unlikely that the Mn

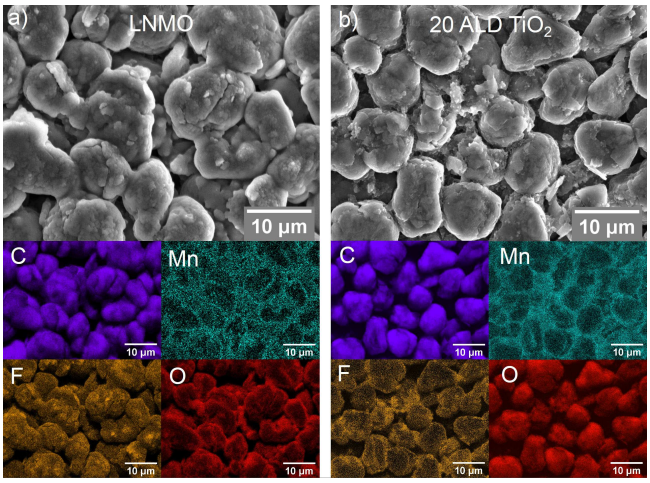

Figure 7. SE images of graphite electrodes after having been cycled against (a) LNMO and (b) 20 ALD TiO_2 for 210 cycles at 20 °C. The EDX elemental maps of C, Mn, F, and O are included for both samples. Scale bars:10 µm.

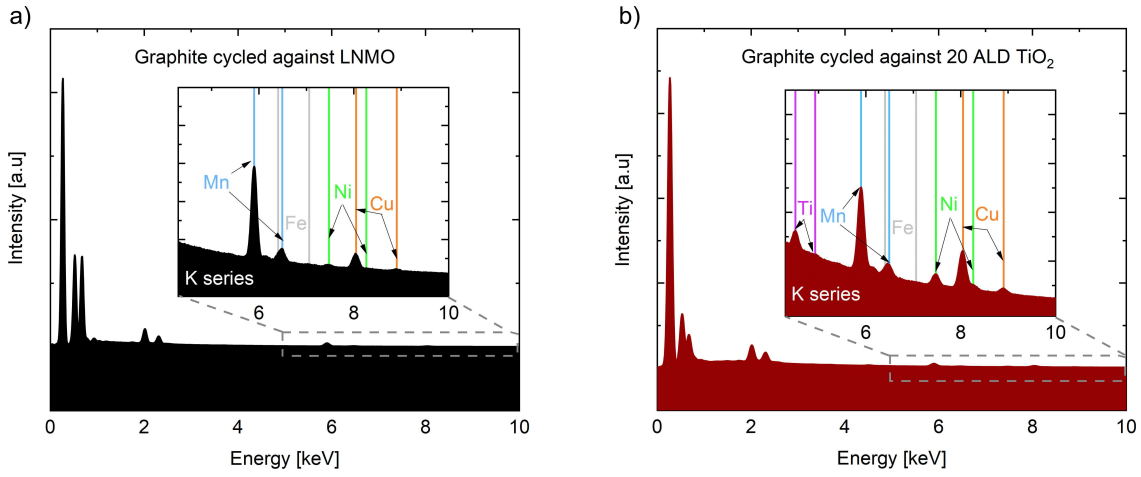

Figure 8. EDX spectra of graphite electrodes cycled 210 cycles against (a) LNMO (black) and (b) 20 ALD TiO_2 (red) at 20 °C.

detected is solely arising from steel corrosion, as the steel alloy contains small amounts of Mn compared to Fe, and the calculated Fe concentration is less than 10 % of the concentration of Mn.

One main difference between the graphite cycled against LNMO and 20 ALD TiO_2 can be observed. In Figure 8b there is a clear Ti peak that is not visible in the LNMO spectrum. The TiO_2-coating has been reported to be offering only temporary protection from HF attack, as it will be fluorinated.[41] Furthermore, Cheng et al.[33] reported that the TiO_2-coating they deposited by ALD on an LCO electrode was no longer detectable by XPS after 5 charging cycles. They attributed the loss of Ti 2p signal to instability due to participation in the redox reactions. There are no signs of similar redox activity from the TiO_2-coating layer based on the electrochemistry data in the current study; however, the XPS results suggests that the TiO_2-layer is fluorinated upon battery cycling. Fluorination of TiO_2-coating on cathode materials has previously been reported by several authors.[32,63] It has furthermore been shown that TiF_4 is soluble in solvents with high donor number.[64] EC, with a donor number of 16.4 kcal mol^{-1},[65] can thus dissolve some TiF_4.

To investigate the extent to which the TiO_2-coating is dissolved during cycling, ICP-MS analysis of a 20 ALD TiO_2 electrode after cycling against graphite for 210 cycles at 20 °C was performed. By comparing the Ti/Mn ratio in this sample to the Ti/Mn ratio in the pristine 20 ALD TiO_2 powder, an estimate to the severity of the Ti dissolution can be made. Even though Mn dissolution has been demonstrated for this sample, it is assumed that the Mn quantity that is lost from the LNMO during cycling is negligible compared to the Mn quantity in the LNMO bulk. The measured Ti and Mn amounts, and corresponding Ti/Mn ratios for both samples are presented in Table 2.

Based on the ICP-MS results there is no change in the Ti/Mn ratio between the two samples within the detectability limit. It can thus be assumed that, even though some of the Ti is dissolving in the electrolyte after 210 charging cycles, most of the Ti still remains on the LNMO surface, protecting the LNMO from HF attack.

As a whole, the results demonstrate the possibilities of TiO_2 as a coating material for LNMO. The increased polarization and reduced discharge capacities for the thicker TiO_2-coatings is a drawback, as it slightly reduces the obtainable energy density of LNMO. However, TiO_2 also shows great promise as it leads to reduced formation of impeding interface layers on both the anode and the cathode, retarded TM dissolution, and improved capacity retention in LNMO||graphite full-cells at 20 °C.

Table 2. ICP-MS results of pristine 20 ALD TIO_2 powder and a 20 ALD TiO_2 electrode cycled against graphite (210 cycles at 20 °C).

Sample	Ti content[a] [mg kg^{-1}]	Mn content[a] [mg kg^{-1}]	Ti/Mn ratio
20 ALD TiO_2 pristine	380	452000	8.4×10^{-4}
20 ALD TiO_2 cycled electrode	384	436000	8.8×10^{-4}

[a] RSD 15–25 %.

Conclusion

Ultra-thin and uniform TiO_2-coating was successfully deposited on $LiNi_{0.5-x}Mn_{1.5+x}O_4$ (LNMO) powder by atomic layer disposition (ALD). Three coating thicknesses of approximately 0.2, 0.3, and 0.6 nm were deposited after 5, 10, and 20 ALD cycles, respectively. X-ray diffraction and Raman spectroscopy revealed no signs of changes in the LNMO bulk due to the coating deposition. The rate capability was slightly worsened at 20 °C by the applied coating, in particular for the thicker TiO_2-coatings due to the Li-diffusion barrier formed by the TiO_2. Little to no improvement in the capacity retention was found from long-term galvanostatic charge-discharge cycling in half-cells, neither at 20 nor at 50 °C. The discharge capacities of the TiO_2-coated samples were, however, improved for the TiO_2-coated samples at 50 °C. Improved capacity retention and coulombic efficiencies were furthermore demonstrated for the TiO_2-coated LNMO at 20 °C in LNMO||graphite full-cells. This improvement in cycling stability can partly be attributed to the reduced formation of impeding cathode electrolyte interphase on the TiO_2-coated sample. Furthermore, the transition metal dissolution after 210 charging cycles was reduced for the TiO_2-coated LNMO, as approximately 3 times lower Mn/C and F/C ratios were found for the graphite cycled against 20 ALD TiO_2, indicating a thinner solid electrolyte interphase. Ti was detected on the graphite cycled against 20 ALD TiO_2 by energy-dispersive X-ray spectroscopy, indicating that the TiO_2-coating is not fully withstanding prolonged cycling. The extent of Ti dissolution is, however, relatively low as no change in the Ti/Mn ratio could be detected by inductively coupled plasma mass spectrometry.

Experimental Section

The active material used as a basis for the current study is LNMO with a chemical composition of $LiNi_{0.43}Mn_{1.57}O_4$, purchased from Haldor Topsøe (Denmark). The cathode active material was coated with TiO_2 with ALD technique in a PICOSUN R-200 Standard ALD system at 120 °C and N_2 gas selected as a carrier gas and purge gas for the titanium tetrachloride ($TiCl_4$) and H_2O precursors. The precursor pulse time was set to 0.2 s at a flow rate of 15 sccm, and the subsequent carrier gas purge duration was set to 5 s at a flow rate of 100 sccm. The procedure was repeated 10 times to obtain a net pulsing time of 2 s for each precursor. In between precursors, the reactor was purged with carrier gas for 60 s at a flow rate of 600 sccm. One growth cycle was achieved after the samples were each exposed to the H_2O and $TiCl_4$ precursors, and 5, 10, and 20 ALD growth cycles were used to prepare samples. 5 ALD TiO_2, 10 ALD TiO_2, and 20 ALD TiO_2 are therefore designated. The vacuum in the reaction chamber was kept to less than 10 hPa.

The bulk LNMO crystal structure was characterized by XRD using a D8 Focus with CuK_α radiation ($\lambda = 1.54$ Å) and LynxEye SuperSpeed Detector. The collection time was 6 h with 2θ-values ranging from 10 to 120°. A crystal structure model with space group *Fd*-3*m* was fitted to the X-ray diffractogram using Topas (Bruker AXS, Version 5). Raman spectroscopy with a lateral resolution of 1–2 μm and probing depth of approximately 100 nm was performed with a Renishaw Raman spectrometer using 532 nm laser, 1200 grating, 50× lens magnification, and 0.5 % laser power. The acquisition time was set to 20 s. The SEM analysis of the LNMO particles was conducted on a Zeiss Ultra 55 limited edition field emission SEM

(FESEM). The LNMO particles were connected to the sample holder with C-tape and analyzed with an acceleration voltage of 5 kV, a working distance of 5.5 mm, and a 30 μm aperture. The BET surface area of the uncoated LNMO powder was measured using a Tristar 3000 Surface area and porosity analyzer. The chemical composition of the samples was analyzed by ICP sector field mass spectrometry (ICP-SFMS) using an ICP-SFMS ELEMENT2 (ThermoScientific, Bremen, Germany). The sample preparation was performed by dissolving the coated and uncoated LNMO powders in a mix of hydrochloric acid, nitric acid, and hydrofluoric acid. ALS Scandinavia AB performed the analysis. The XPS analysis of the LNMO powders was carried out on an Axis Ultra DLD X-ray photoelectron spectrometer with a monochromatic Al-K_α X-ray source (10 mA, 10 kV). Regional maps with higher resolution were collected with a 0.1 eV step size. All data analysis was performed using CasaXPS software with Shirley background subtraction. The data was energy calibrated to the hydrocarbon peak (285 eV). The TEM specimens were prepared with a Helios G4 dual-beam focused ion beam (FIB)-SEM instrument. Several adjacent LNMO particles were covered and weld together with electron- and ion-deposited carbon. The particles were attached to a Cu half-grid individually and thinned by a Ga-ion beam. The final thinning was done with 2 kV ions. STEM was carried out by a JEOL ARM-200F image- and probe-corrected microscope, using a voltage of 200 kV, a beam current of 80 pA, a convergence angle of 27 mrad, and an annular dark-field detector with inner collection angle 35 mrad. EELS was performed with a GIF Quantum spectrometer. A 35 mrad collection angle and 0.5 or 1 eV dispersion were used. Single frame chemical maps were acquired with 10 ms dwell time.

Electrode coatings for all samples were produced by mixing 90 wt% LNMO, 5 wt% carbon black (Imerys C-nergy Super C 65) and 5 wt% PVDF (Kynar Flex HFP2801) in solution [*N*-methyl-2-pyrrolidone (NMP) solvent] using a Retsch MM400 shaker mill with three ZrO_2-balls (5 mm) at 25 Hz for 20 min. This soft slurry mixing approach was used to avoid damaging the ALD TiO_2-coating and breakage of the secondary LNMO particles. The slurry was coated on to 22 μm thick carbon-coated Al foil (SDX, ShowaDenko). The gap size of the coating bar was varied according to the desired active mass loading. A gap size of 150 μm was used for half-cell electrodes yielding a loading of approximately 5 mg cm^{-2}, and a 200 μm gap size was used for full-cell electrodes yielding a loading of approximately 7.5 mg cm^{-2}. Electrodes were dried overnight at 60 °C, before disc-shaped electrodes of 12 and 16 mm were cut (for half- and full-cells, respectively) and further densified at 15–20 MPa for 3 min using a uniaxial press. Before cell assembly, the electrodes were dried at 120 °C under dynamic vacuum for 12 h. before they were transferred to an Ar-filled glovebox (O_2 and H_2O levels <0.1 ppm) where the CR-2032 coin cells were assembled. Celgard 2325 separator was used for all cells. Li foil (0.75 mm, Alfa Aesar) or commercial graphite anodes (1.1 mAh cm^{-2}, CustomCells) were used as counter electrodes. 40 μL (50 μL) electrolyte (1 M $LiPF_6$ in EC/DEC = 50:50 (*v*/*v*), Sigma–Aldrich) was added to each half (full) cell by micropipette. The spacer thickness was 0.5 mm for half-cells and 1 mm for full-cells. After a 10 h rest step, long-term galvanostatic cycling and rate testing was conducted using a LAND battery testing system (CT2001A) and Bio-Logic BCS-805 in a temperature-controlled room (20 °C) or in a temperature chamber (50 °C). The long-term cycling was conducted with C-rates of 0.5 C with two charge-discharge cycles of 0.1C every 25th charge cycle. The half-cell rate testing was conducted with 5 cycles of C/10, C/5, C/2, 1C, 2C, and finally C/10. 1C corresponds to a current of 140 and 130 mAh g^{-1} for half- and full-cell testing, respectively. All full-cells are balanced with an overdimentioned graphite electrode to avoid Li plating. The graphite capacity was 1.1 mAh cm^{-2} while the LNMO capacity was aimed to be around 0.95 mAh cm^{-2}, yielding an N/P capacity ratio of approximately 1.16, where 1 C corresponds to 130 mAh g^{-1}.[66]

In preparation for all post-mortem characterization, the cells were opened in an Ar-filled glovebox, and the electrodes were extracted and rinsed 3 times with dimethyl carbonate (DMC) and left to dry. They were transported from the glove box in a sealed, Ar-filled container. In the case of the EDX analysis of the graphite electrodes, the electrodes were exposed to air for a maximum of 1 min during sample transfer. The EDX analysis of the graphite electrodes was conducted with a Hitachi S-3400 N SEM equipped with an Oxford EDX system. The SE images and data were collected in a voltage range of 13 to 17 keV. The EDX data was analyzed with the Aztec Software using the TruMap function displayed in at %.

The XPS analysis of the electrodes was carried out with a Kratos Axis Ultra spectrometer using a monochromatic Al K_α source (120 W). The samples were mounted on carbon tape and the analysis area is approximately 300×700 μm^2. Samples were transferred from the glove box to XPS equipment chamber using an air sensitive transport arm filled with Argon. A pass energy of 80 eV was used for survey scans and 40 eV for the core level regions. Data calibration was performed by shifting the highest intensity position of the main Mn 2p peak to 642.3 eV, as illustrated in Figure S9 (Supporting Information). The hydrocarbon peak (C 1 s peaks are included in Figure S9, Supporting Information) was not chosen as a basis for energy calibration due to the relative BE shifts that are known to occur at different states of charge (SOCs), making energy calibration challenging.[67] Even though Mn partly contributes to the capacity in LNMO, it is expected to be less active than other LNMO components during most of the delithiation process. Mn 2p was therefore chosen as a bulk specific internal reference.[47] The CASA XPS software was applied to analyze the spectra by subtracting a Shirley-type background.

Acknowledgements

The authors acknowledge and thank Dr. Julian Tolchard and Dr. Sigurd Wenner in SINTEF Industry for valuable assistance in sample preparation, characterization, and data analysis by EDX and TEM, respectively. Assoc. Prof. Erik Lewin at Uppsala University is acknowledged for access to the ALD reactor. This work is performed within MoZEES, a Norwegian Centre for Environment friendly Energy Research (FME), co-sponsored by the Research Council of Norway (project number 257653) and 40 partners from research, industry, and public sector. The FIB work was done within the Norwegian Micro- and Nano-Fabrication Facility, NorFab (RCN, grant 245963/F50). The TEM work was carried out at the NORTEM (RCN, grant 197405) infrastructure at the TEM Gemini Centre, Trondheim, Norway. In addition, Yonas Tesfamhret and Daniel Brandell acknowledge STandUP for Energy.

Conflict of Interest

The authors declare no conflict of interest.

Data Availability Statement

The data that support the findings of this study are available from the corresponding author upon reasonable request.

Keywords: cathode materials · electrochemistry · energy conversion · lithium-ion battery · sustainable chemistry

[1] G. Liang, V. K. Peterson, K. W. See, Z. Guo, W. K. Pang, *J. Mater. Chem. A* **2020**, *8*, 15373–15398.
[2] M. Wentker, M. Greenwood, J. Leker, *Energies* **2019**, *12*, 504.
[3] K. Xu, *Chem. Rev.* **2014**, *114*, 11503–11618.
[4] M. He, L. Boulet-Roblin, P. Borel, C. Tessier, P. Novák, C. Villevieille, E. J. Berg, *J. Electrochem. Soc.* **2016**, *163*, A83–A89.
[5] Q. Li, Y. Wang, X. Wang, X. Sun, J. Zhang, X. Yu, H. Li, *ACS Appl. Energ. Mater.* **2020**, *12*, 2319–2326.
[6] Y. Zhang, Y. Katayama, R. Tatara, L. Giordano, Y. Yu, D. Fraggedakis, J. G. Sun, F. Maglia, R. Jung, M. Z. Bazant, Y. Shao-Horn, *Energy Environ. Sci.* **2020**, *13*, 183–199.
[7] N. P. W. Pieczonka, Z. Liu, P. Lu, K. L. Olson, J. Moote, B. R. Powell, J.-H. Kim, *J. Phys. Chem. C* **2013**, *117*, 15947–15957.
[8] M. S. Whittingham, *Chem. Rev.* **2004**, *104*, 4271–4301.
[9] L. Hanf, J. Henschel, M. Diehl, M. Winter, S. Nowak, *Electrophoresis* **2020**, *41*, 697–704.
[10] N. N. Intan, K. Klyukin, V. Alexandrov, *ACS Appl. Mater. Interfaces* **2019**, *11*, 20110–20116.
[11] A. Jarry, S. Gottis, Y.-S. Yu, J. Roque-Rosell, C. Kim, J. Cabana, J. Kerr, R. Kostecki, *J. Am. Chem. Soc.* **2015**, *137*, 3533–3539.
[12] T. F. Yi, J. Mei, Y. R. Zhu, *J. Power Sources* **2016**, *316*, 85–105.
[13] U. Nisar, N. Muralidharan, R. Essehli, R. Amin, I. Belharouak, *Energy Storage Mater.* **2021**, *38*, 309–328.
[14] J. W. Kim, D. H. Kim, D. Y. Oh, H. Lee, J. H. Kim, J. H. Lee, Y. S. Jung, *J. Power Sources* **2015**, *274*, 1254–1262.
[15] S. Tao, F. Kong, C. Wu, X. Su, T. Xiang, S. Chen, H. Hou, L. Zhang, Y. Fang, Z. Wang, W. Chu, B. Qian, L. Song, *J. Alloys Compd.* **2017**, *705*, 413–419.
[16] X. Hao, B. M. Bartlett, *J. Electrochem. Soc.* **2013**, *160*, A3162–A3170.
[17] U. Nisar, S. A. J. A. Al-Hail, R. K. Petla, R. A. Shakoor, R. Essehli, R. Kahraman, S. Y. AlQaradawi, D. K. Kim, I. Belharouak, M. R. Amin, *ACS Appl. Energ. Mater.* **2019**, *2*, 7263–7271.
[18] E. R. Østli, Y. Tesfamhret, S. Wenner, M. J. Lacey, D. Brandell, A. M. Svensson, S. M. Selbach, N. P. Wagner, *ACS Omega* **2021**, *6*, 30644–30655.
[19] M. V. Koudriachova, N. M. Harrison, S. W. de Leeuw, *Solid State Ionics* **2003**, *157*, 35–38.
[20] M. Wagemaker, R. Van de Krol, A. P. M. Kentgens, A. A. Van Well, F. M. Mulder, *J. Am. Chem. Soc.* **2001**, *123*, 11454–11461.
[21] H. T. Fang, M. Liu, D. W. Wang, T. Sun, D. S. Guan, F. Li, J. Zhou, T. K. Sham, H. M. Cheng, *Nanotechnology* **2009**, *20*, 225701.
[22] G. Armstrong, A. R. Armstrong, P. G. Bruce, P. Reale, B. Scrosati, *Adv. Mater.* **2006**, *18*, 2597–2600.
[23] M. Pfanzelt, P. Kubiak, M. Fleischhammer, M. Wohlfahrt-Mehrens, *J. Power Sources* **2011**, *196*, 6815–6821.
[24] S. Hao, C. Wolverton, *J. Phys. Chem. C* **2013**, *117*, 8009–8013.
[25] H. H. Pham, L. W. Wang, *Phys. Chem. Chem. Phys.* **2015**, *17*, 541–550.
[26] M. Zhang, G. Lin, C. Dong, L. Wen, *Surf. Coat. Technol.* **2007**, *201*, 7252–7258.
[27] C. Fares, F. Ren, M. J. Tadjer, J. Woodward, M. A. Mastro, B. N. Feigelson, C. R. Eddy, S. J. Pearton, *Appl. Phys. Lett.* **2020**, *117*, 182103.
[28] X. Liang, M. Huang, Y. Zhao, H. Wu, Y. Wang, F. Tang, *Int. J. Electrochem. Sci.* **2016**, *11*, 4611–4618.
[29] R. W. Johnson, A. Hultqvist, S. F. Bent, *Mater. Today* **2014**, *17*, 236–246.
[30] X. Meng, *J. Mater. Res.* **2021**, *36*, 2–25.
[31] W. Lu, L. Liang, X. Sun, X. Sun, C. Wu, L. Hou, J. Sun, C. Yuan, *Nanomaterials* **2017**, *7*, 325.
[32] A. Zhou, Y. Lu, Q. Wang, J. Xu, W. Wang, X. Dai, J. Li, *J. Power Sources* **2017**, *346*, 24–30.
[33] H. M. Cheng, F. M. Wang, J. P. Chu, R. Santhanam, J. Rick, S. C. Lo, *J. Phys. Chem. C* **2012**, *116*, 7629–7637.
[34] C. Qin, J. Cao, J. Chen, G. Dai, T. Wu, Y. Chen, Y. Tang, A. Li, Y. Chen, *Dalton Trans.* **2016**, *45*, 9669–9675.
[35] J. Lu, C. Zhan, T. Wu, J. Wen, Y. Lei, A. J. Kropf, H. Wu, D. J. Miller, J. W. Elam, Y. K. Sun, X. Qiu, K. Amine, *Nat. Commun.* **2014**, *5*, 5693..
[36] F. Mattelaer, P. M. Vereecken, J. Dendooven, C. Detavernier, *Adv. Mater. Interfaces* **2017**, *4*, 1601237..
[37] J. Kim, H. Kim, K. Kang, *J. Korean Ceram. Soc.* **2018**, *55*, 21–35.
[38] H. Wang, L. Ben, H. Yu, Y. Chen, X. Yang, X. Huang, *J. Mater. Chem. A* **2017**, *5*, 822–834.
[39] S. Tao, F. Kong, C. Wu, X. Su, T. Xiang, S. Chen, H. Hou, L. Zhang, Y. Fang, Z. Wang, W. Chu, B. Qian, L. Song, *J. Alloys Compd.* **2017**, *705*, 413–419.
[40] H. Cho, M. V. Chen, A. C. Macrae, Y. S. Meng, *Appl. Mater. Interf.* **2015**, *7*, 16231–16239.
[41] L. Ben, H. Yu, Y. Wu, B. Chen, W. Zhao, X. Huang, *ACS Appl. Energ. Mater.* **2018**, *1*, 5589–5598.
[42] M. Chaudhary, S. Tyagi, R. K. Gupta, B. P. Singh, R. Singhal, *Surf. Coat. Technol.* **2021**, *412*, 127009.
[43] E. Björklund, D. Brandell, M. Hahlin, K. Edström, R. Younesi, *J. Electrochem. Soc.* **2017**, *164*, A3054–A3059.
[44] J. Betz, J. P. Brinkmann, R. Nölle, C. Lürenbaum, M. Kolek, M. C. Stan, M. Winter, T. Placke, *Adv. Energy Mater.* **2019**, *9*, 1900574.
[45] B. Aktekin, M. Valvo, R. I. Smith, M. H. Sørby, F. Lodi Marzano, W. Zipprich, D. Brandell, K. Edström, W. R. Brant, *ACS Appl. Energ. Mater.* **2019**, *2*, 3323–3335.
[46] L. Boulet-Roblin, C. Villevieille, P. Borel, C. Tessier, P. Novák, M. Ben Yahia, *J. Phys. Chem. C* **2016**, *120*, 16377–16382.
[47] B. Aktekin, F. Massel, M. Ahmadi, M. Valvo, M. Hahlin, W. Zipprich, F. Marzano, L. Duda, R. Younesi, K. Edström, D. Brandell, *ACS Appl. Energ. Mater.* **2020**, *3*, 6001–6013.
[48] O. Anderson, C. R. Ottermann, R. Kuschnereit, P. Hess, K. Bange, *Fresenius J. Anal. Chem.* **1997**, *358*, 315–318.
[49] D. Saha, R. S. Ajimsha, K. Rajiv, C. Mukherjee, M. Gupta, P. Misra, L. M. Kukreja, *Appl. Surf. Sci.* **2014**, *315*, 116–123.
[50] C. Jin, B. Liu, Z. Lei, J. Sun, *Nanoscale Res. Lett.* **2015**, *10*, 95–103.
[51] Y.-F. Deng, S. X. Zhao, P.-Y. Zhai, G. Cao, C.-W. Nan, *J. Mater. Chem. A* **2015**, *3*, 20103–20107.
[52] T.-F. Yi, J. Mei, Y.-R. Zhu, *J. Power Sources* **2016**, *316*, 85–105.
[53] R. Younesi, G. M. Veith, P. Johansson, K. Edström, T. Vegge, *Energy Environ. Sci.* **2015**, 1905–1922.
[54] K. Tasaki, K. Kanda, S. Nakamura, M. Ue, *J. Electrochem. Soc.* **2003**, *150*, A1628.
[55] J. H. Kim, N. P. W. Pieczonka, Z. Li, Y. Wu, S. Harris, B. R. Powell, *Electrochim. Acta* **2013**, *90*, 556–562.
[56] D. S. Lu, L. B. Yuan, J. L. Li, R. Q. Huang, J. H. Guo, Y. P. Cai, *J. Electroanal. Chem.* **2015**, *758*, 33–38.
[57] B. Aktekin, M. J. Lacey, T. Nordh, R. Younesi, C. Tengstedt, W. Zipprich, D. Brandell, K. Edstrom, *J. Phys. Chem. C* **2018**, *122*, 11234–11248.
[58] A. N. Mansour, D. G. Kwabi, R. A. Quinlan, Y.-C. Lu, Y. Shao-Horn, *J. Electrochem. Soc.* **2016**, *163*, A2911–A2918.
[59] R. A. Quinlan, Y.-C. Lu, Y. Shao-Horn, A. N. Mansour, *J. Electrochem. Soc.* **2013**, *160*, A669–A677.
[60] M. He, Z. Wang, X. Yan, L. Tian, G. Liu, X. Chen, *J. Power Sources* **2016**, *306*, 309–316.
[61] K. Edström, M. Herstedt, D. P. Abraham, *J. Power Sources* **2006**, *153*, 380–384.
[62] S. Leroy, F. Blanchard, R. Dedryvère, H. Martinez, B. Carré, D. Lemordant, D. Gonbeau, *Surf. Interface Anal.* **2005**, *37*, 773–781.
[63] L. Su, S. K. Jha, X. L. Phuah, J. Xu, N. Nakamura, H. Wang, J. S. Okasinski, B. Reeja-Jayan, *J. Mater. Sci.* **2020**, *55*, 12177–12190.
[64] G. B. Nikiforov, C. Knapp, J. Passmore, A. Decken, *J. Fluorine Chem.* **2006**, *127*, 1398–1404.
[65] S. S. Sekhon, N. Arora, H. P. Singh, *Solid State Ionics* **2003**, *160*, 301–307.
[66] J. Kasnatscheew, T. Placke, B. Streipert, S. Rothermel, R. Wagner, P. Meister, C. Laskovic, M. Winter, *J. Electrochem. Soc.* **2017**, *164*, A2479–A2486.
[67] F. Lindgren, D. Rehnlund, I. Källquist, L. Nyholm, K. Edström, M. Hahlin, J. Maibach, *J. Phys. Chem. C* **2017**, *121*, 27303–27312.

Manuscript received: February 14, 2022
Revised manuscript received: April 8, 2022
Accepted manuscript online: April 19, 2022
Version of record online: May 12, 2022